AIAA AVIATION Forum
13-17 June 2016, Washington, D.C.
46th AIAA Fluid Dynamics Conference

10.2514/6.2016-4103

Analysis of Hypersonic Flow Effects on Sensor Performance

Lauren E. Mackey[1] and Iain D. Boyd[2]
University of Michigan, Ann Arbor, MI 48109

A potential future use of hypersonic platforms is for responsive Intelligence, Surveillance, and Reconnaissance (ISR). It is common for these types of missions to employ Electro-Optical/Infrared (EO/IR) sensors and Radio Frequency (RF) sensors to collect information. Analysis is needed to assess sensor performance while traveling at hypersonic speeds, especially in the turbulent regime. Such flows create density gradients and may degrade EO/IR sensor performance. The strong shock waves that surround hypersonic vehicles can promote the formation of plasma sheathes. These sheathes can obscure RF signals, potentially making them unusable. A significant effect on sensors can also come from the surface temperature. If the temperature exceeds certain thresholds, the portion of the sensor exposed to the flow could suffer damage and/or performance loss. In this study, numerical simulations are utilized to examine the effects of hypersonic flow on sensor signal degradation. The simulations are performed at Mach 7 and an altitude of 30 km on an axisymmetric cone. These conditions represent a unit Reynolds number of 2.56×10^6 m^{-1} which suggests the associated boundary layer is likely to be turbulent. The results show that computational methods can be helpful in assessing signal degradation. However, there is a need to expand the existing methods of analysis.

Nomenclature

Rs	=	Strehl ratio
OPD	=	Optical Path Difference [m]
n	=	Index of refraction
δ	=	Boundary layer thickness [m]
C_f	=	Skin friction coefficient
k	=	Wave number [m^{-1}]
λ	=	Wave length [m]
T	=	Temperature [K]
p	=	Pressure [Pa]
Ψ	=	Phase error,
ρ	=	Density [kg/m^3]
L	=	Length between 5% and 95% of the index of refraction profile [m]
β	=	Gladstone-Dale constant [m^3/kg]
σ	=	Correction factor
C_w	=	Experimentally or computationally derived correction factor
r_2	=	Temperature relation
f	=	Frequency [Hz]
κ	=	Attenuation per unit length [dB/m]
b^3/a	=	Experimentally derived constant
y	=	Coordinate along line of sight [m]

Subscripts

∞	=	Freestream
ref	=	Reference
radio	=	Pertaining to radio waves
critical	=	Pertaining to critical plasma density

[1] Ph.D. Candidate, Department of Aerospace Engineering, Student Member AIAA.
[2] James E. Knott Professor of Engineering, Department of Aerospace Engineering, Fellow AIAA.

p = Plasma
rms = Root mean square

I. Introduction

TRADITIONAL means of sensing for applications in the field of Intelligence, Surveillance, and Reconnaissance (ISR) may be rendered unusable by the physical phenomena associated with hypersonic flow. Previously, sensors have mostly been subjected to the flow physics associated with sub and super-sonic flows. As Mach number increases, however, differing flow characteristics must be considered as they gain importance. Hypersonic flight is likely to experience high temperatures and strong shocks. These phenomena cause non-equilibrium flow which can further obscure sensors and must be included to accurately determine hypersonic sensor performance.

Including the real gas effects is integral to calculating Radio Frequency (RF) sensor degradation. Radio blackout can only be accounted for when ionization is considered. Radio blackout occurs when there is enough energy imparted onto the molecules surrounding the vehicle that they ionize. Radio waves can be reflected or diminished as they travel through this plasma field.[4] In fact, any signal will be attenuated for frequencies that fall below the plasma frequency.[1] Low frequency RF waves are the most vulnerable. Radio blackout is a problem that has plagued many vehicles associated with space travel. The Apollo missions experienced many minutes of lost communications, for example.[1] This continued to be an issue even for the more modern Space Shuttle missions.[1] While the ISR platforms are intended to fly intra-atmospheric missions, blackout may still be an issue since these vehicles will experience strong shock waves with elevated temperatures.

At hypersonic Mach numbers, vehicle surface temperatures become elevated. This is due to the viscous interaction of the fluid with the vehicle. High Mach flow carries large amounts of kinetic energy. The flow must be slowed at the wall to zero velocity. This creates a large transfer of energy. One way this transfer of energy manifests itself is as an increase in vehicle surface temperature. The flow considered in this study is also turbulent. An important part of turbulence is increased mixing. This mixing promotes the transfer of both momentum and energy which further increases surface temperature.

The final aspect of sensing that needs to be addressed is optical and infrared distortions. These, perhaps, may be the most difficult to quantify computationally. EO/IR signals can become abberated as the waves traverse a field that has changing density. As the wave fronts travel through the changing density field, portions travel at different speeds, thus obscuring the signal. Turbulent fluctuations can create an even more varied density field. It is important to consider these effects as well. Most research in this area has been confined to experimentation.[2, 3, 17] Computational research has centered mostly on higher fidelity methods (LES, etc.).[13] Because of this, the computations conducted are at low Reynolds numbers and over simple geometries.[3] Some Reynolds Averaged Naiver-Stokes (RANS) calculations have also been conducted, but the previous simulations are limited in scope.[3]

This paper will explore all three types of aberrations. It will describe the numerical approaches taken to analyze each. It should be noted that two methods are used to predict the optical distortion, one of which is designed to specifically handle turbulent flows. The paper will quantify the effects on sensors that the flow will have. The results are divided into three sections; one for each of the topics discussed above. In the final section of the paper conclusions are presented that assess the methods used and ways to improve and expand them in the future.

II. Technical Approach

This study employs the University of Michigan's hypersonic computational fluid dynamics (CFD) code LeMANS. LeMANS is a solver that can simulate flows that are weakly in thermo-chemical non-equilibrium by assuming the flow is approximately continuum.[5] This type of flow is often experienced during hypersonic flight where the air molecules can be in excited modes due to the extreme physical conditions. In order to solve for flow conditions LeMANS couples the Navier-Stokes equations with thermodynamic and transport property models. [5] Also included in the code are models for finite rate chemistry and energy relaxation models.[5] LeMANS works by taking the differential equations and integrating these equation spatially and temporally. To integrate spatially, the finite volume method is implemented. Fluxes across each cell are calculated using a flux vector splitting scheme for the inviscid components and a central scheme for the viscous parameters. [5] Furthermore, it is assumed that the fluid is Newtonian, and the shear stress can be calculated using Stokes' hypothesis.

In order to examine the boundary layers critical to the present study, three turbulence models are added to LeMANS: Menter BSL[6], Menter SST[6], and Spalart-Allmaras.[7] The original code is modified to solve the RANS equations when the flow is assumed to be turbulent. The computational methods employed for the turbulence models are similar to those in the laminar code. For the cases that are of interest in this study, the flow is assumed to be completely turbulent. Once the flow data is calculated, various parameters along various linear paths,

representing lines-of-sight, and along the vehicle surface, are evaluated to assess how sensors performance would be affected.

A. EO/IR Interference

1. Method 1

Many ISR vehicles use EO/IR sensors that collect electro-magnetic signals. EO/IR signals can experience degradation due to the boundary layer surrounding the vehicle.[8] This degradation is characterized by the Strehl ratio which describes the ratio of the focused intensity of the disturbed beam to a "perfect" undisturbed beam. Therefore, an undistorted beam would have a Strehl ratio equal to one. The ratio is calculated by analyzing the index-of-refraction fluctuations, designated by the phase error.[9] The Strehl (Rs) ratio can be calculated using:

$$Rs = \exp(-<\Psi^2>) \tag{1}$$

where Ψ is the phase error. The phase error can be calculated using Eq. (2).[9] It should be noted that this model is designed to analyze turbulent disruptions to the signal in free shear flows. However, it is assumed here that it can provide general trends when care is taken to ensure that the physics of the boundary layer are retained.

$$<\Psi^2> = 2k^2\left(\frac{b^3}{a}\right)L^3\int\left(\frac{dn}{dy}\right)^2 dy \tag{2}$$

In Eq. (2), k is the wave number, b^3/a is an experimentally determined value of 0.0057, n is the index of refraction, and L is the lateral distance between the 5% and 95% values of the time-averaged index of refraction profiles.[10] Because this model is designed to work for free shear flows and not for features such as shocks, only the profile of n near the wall is used.

In order to obtain Rs, one needs to know the index of refraction spatial profile. This is evaluated using Eq. (3) as a function of coordinate y:[8]

$$n = 1 + \beta\left(\frac{\rho(y)}{\rho_{ref}}\right) \tag{3}$$

where β is a mass averaged Gladstone-Dale constant, ρ is the mass density, and ρ_{ref} is the reference mass density at 1 Atm and 273 K. The Gladstone-Dale constant is not readily available in the literature for chemically reacting cases. However, for the cases tested, the chemistry did not play an important part in the overall flow; the density of the reactants never exceeds 10^{-8} kg/m^3. Because of the relative unimportance of chemistry, the index of refraction of air as provided by Ref. 11 is used. This information is provided for a temperature of 15°C and a pressure of 1 Atm and is plotted in Fig. 2 over wavelengths of interest. A correction is provided in Ref. 11 to account for variations in temperature and pressure:

$$\sigma_{correction} = p\frac{[1 + p(60.1 - 0.972T)10^{-10}]}{96095.43(1 + .0003661T)} \tag{4}$$

In Eq. (4), $\sigma_{correction}$ is the correction multiplier, p is the pressure in Pascals and T is the temperature in degrees Celsius. The temperature and pressure profiles are calculated in LeMANS. The correction profile is multiplied by the index of refraction to obtain an index of refraction profile. The gradient of the index of refraction is integrated to find the Strehl ratio.

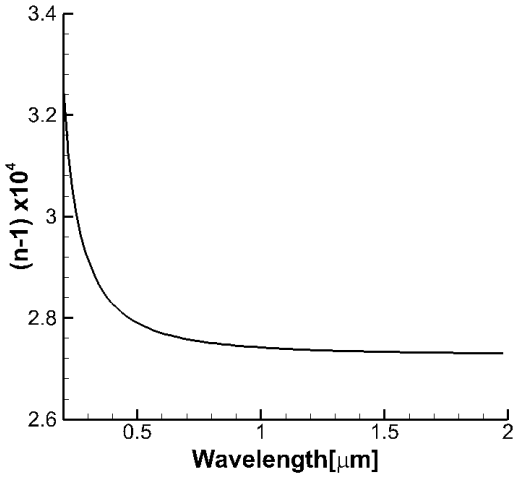

Figure 1. Index of Refraction at various wavelengths.

2. Method 2

The method described above does not take any turbulent fluctuations into consideration. In order to better assess flows with turbulent fluctuations, an equation derived by Wyckham and Smits[2] is adapted to capture the effects of the larger eddies which are present outside of the near-wall region in turbulent flow. In their work, they assumed that the optical aperture is larger than the boundary layer thickness. This compared well to experimental measurements at Strehl ratios greater than 0.3.[2] When the Strehl ratio is expected to be below 0.3, Method 2 can provide worst case scenario results. Their analysis began with defining the rms optical path difference (OPD) using:

$$OPD_{rms} = \int_0^L n' dy = \int_0^L \beta \rho' dy \tag{5}$$

where n' is the fluctuation in the index of refraction, ρ' is the fluctuating density, and β is the Gladstone-Dale constant. The OPD is the difference between the optical path length and the spatially averaged optical path length. The integral was further simplified using the strong Reynolds analogy and the ideal gas law to the following form:

$$OPD_{rms} = \beta \rho_\infty \int_0^L (\gamma - 1) M_\infty^2 \sqrt{\frac{C_f}{2}} \left(\frac{T_\infty U_\infty}{TU} \sqrt{\frac{\rho_\infty}{\rho}} \right) \sqrt{\frac{\overline{\rho u'}}{\tau_w}} dy \tag{6}$$

where C_f is the skin friction coefficient, τ_w is the shear stress at the wall, γ is the specific heat ratio, and M_∞ is the freestream Mach number. It was assumed that the integral could be solved by averaging the variables over the path of interest. This was accomplished by relating the variables to their corresponding freestream values. For example, the average velocity was set to be 0.8 of the freestream velocity since this is the speed that the large scale turbulent eddies convect at. Gordeyev showed that this approximation, and the convective velocity of the large scale motions, can vary with Mach.[16] The velocity multiplier did not vary too greatly, so the original value is used in these calculations. After all of the scaling arguments were made, Eq. (6) was reduced to the following form:

$$OPD_{rms} = C_w r_2^{-\frac{2}{3}} M_\infty^2 \beta \sqrt{C_f} \rho_\infty \delta \tag{7}$$

where C_w is experimentally determined to be approximately 0.7, δ is the boundary layer thickness, C_f is the skin friction coefficient, and r_2 is calculated for a non-adiabatic wall using:

$$r_2 = \frac{1}{2}\left(\frac{T_w}{T_\infty} + 1\right) \tag{8}$$

where T_w is the wall temperature and T_∞ is the freestream temperature. Equation (7) has been shown to compare well to experimental data.[2] It should be noted that Eq. (7) is derived for a line of sight that is normal to the wall. Adjustments to the line of sight length will be made to estimate the distortion along non-perpendicular paths. This

estimate will not include the anisotropic features of the turbulent flow. In order to include these features, detailed information about the turbulent density fluctuations would need to be known. The final step in this method is to find the Strehl ratio using:

$$Rs = \exp\left(-\left(\frac{2\pi OPD_{rms}}{\lambda}\right)^2\right) \tag{9}$$

where λ is wavelength.

Instead of applying this formula with the experimental value of C_w, the case utilized in Ref. 2 is simulated using LeMANS. The experiment consisted of a flat plate in Mach 7.7 air. The reported wall temperature is half of the adiabatic wall temperature.[2] The stagnation temperature and pressure were provided in Ref. 2 and are 700 K and 9.2 MPa, respectively. It was assumed in the experiment that the isentropic relations can be used to find the static temperature in the core of the flow. This assumption is replicated in the numerical simulation. The static pressure altitude is provided and is 30 km.[2] This case is run using the Menter-SST turbulence model since the experimental Reynolds number (18×10^6 m^{-1}) puts the simulation well within the turbulent regime. The computation is run on a mesh with approximately 20,000 cells. The wall y+ is below 0.5 for the entire length of the wall. The simulation took a total time of 100 CPU hours.

Contours of density and Mach are shown in Fig. 2 to illustrate the key aspects of this flow field.

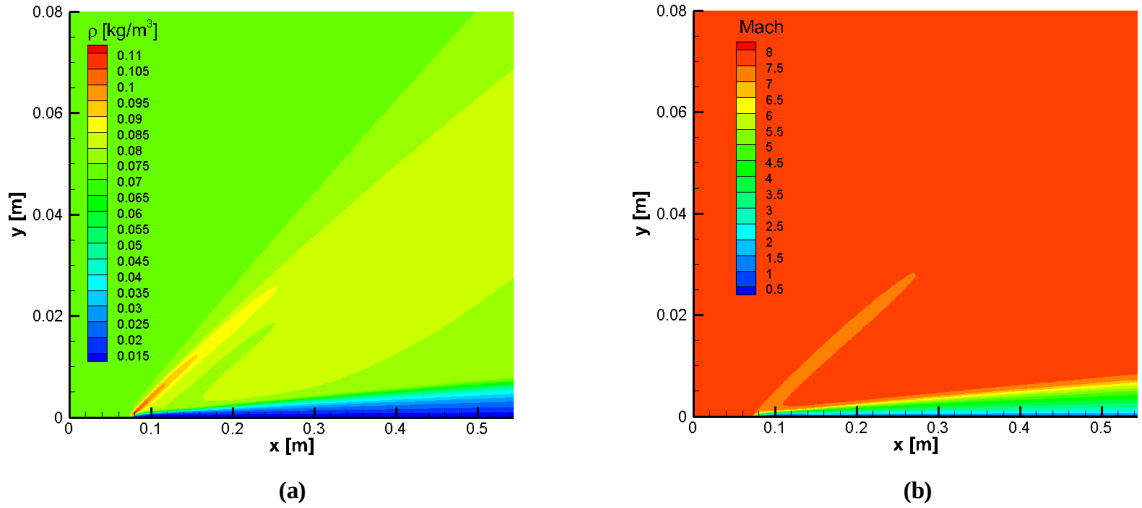

(a) **(b)**

Figure 2. Flat plate density (a) and Mach (b) profiles

As can be seen in Fig. 2, the flow is typical of a hypersonic, high Reynolds number, flat plate case. It consists of a relatively weak oblique shock at the leading edge of the plate and a thin boundary layer confined to the area near the wall. With this flow data calculated, the constant is found by rearranging Eq. (7) for C_w, as shown in Eq. (10):

$$C_w = \frac{OPD_{rms}}{r_2^{-\frac{2}{3}} M_\infty^2 \beta \sqrt{C_f} \rho_\infty \delta} \tag{10}$$

All values required in Eq. (10) are calculated from LeMANS, except for the OPD which is found in the experiment. The boundary layer thickness is located at the y-coordinate where the flow velocity is 99% of the freestream value. All of the variables needed for evaluation of Eq. (10) are extracted at the x location of 0.356 m to be consistent with the experiment. The calculated value of C_w is 0.93. It should be noted that for visible wavelengths, the Gladstone-Dale constant takes the value of 2.27×10^{-4} m^3/kg. The value of the Gladstone-Dale constant for infrared signals is derived by dividing the corrected n-1 profile by the density profile according to Eq. (3).[11] This provides a value of 2.23×10^{-4} m^3/kg. This approach will account for any differences in the experimental and computational data, and hence allow the proper Strehl ratio to be inferred from computational analysis.

This method is derived for a flow with no pressure gradient in the direction normal to the wall. In the hypersonic vehicle analyzed later in the study, the surface possesses a slight curvature. When analyzing this type of geometry, a

pressure gradient in the normal direction is present in the governing equations. After completing an order of magnitude analysis and integrating over the boundary layer, it is found that this pressure gradient is proportional to the ratio of the boundary layer thickness to the radius of curvature of the surface.[15] This shows that the pressure gradient is still negligible if the boundary layer thickness is much smaller than the radius of curvature. For this study, the geometry in question fulfills this requirement as long as the line of sight is not close to the nose of the vehicle. Therefore, as long as the data is taken in an area that is sufficiently far from the nose, Eq. (7) can still be applied.

B. RF Sensors

A vehicle traveling at hypersonic speeds will experience strong shocks creating high flow temperatures. A plasma sheath can then form around the vehicle resulting in radio blackout. This would cause any of the signals sent or collected by the vehicle to be degraded. The analysis of radio blackout involves finding the critical plasma density above which the signal will become distorted, see Eq. (11).[1]

$$n_{critical} = \left(\frac{f_{radio}}{8.985}\right)^2 \tag{11}$$

where f_{radio} is the frequency of the RF sensor. Figure 3 shows the critical density over a common range of operational radio frequencies. If a signal experiences degradation, then the attenuation per unit length can be calculated using Eq. (12).[1]

$$\kappa = 1.821\ x\ 10^{-7}\sqrt{80.255 n_p - f_{radio}} \tag{12}$$

where n_p denotes the plasma number density.

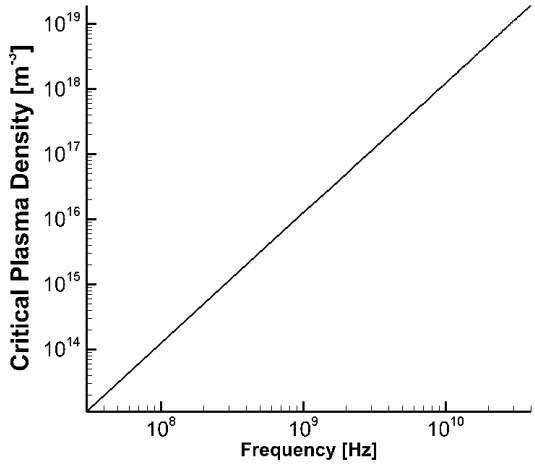

Figure 3. Critical plasma density for various RF frequencies

Common frequencies used in sensing applications can range anywhere from 0.03 to 40 GHz. Table 1 summarizes these sensor frequency ranges.

Table 1. Radio frequency ranges and uses[1]

Frequency Range	Use
0.03 - 0.3 GHz	Voice communications
0.3 - 3.0 GHz	Data Telemetry and Voice communications
1.0 - 2.0 GHz	GPS
2.0 - 4.0 GHz	Data telemetry
8 – 12 GHz	Data and Satellite communication
27 – 40 GHz	Radar and experimental communication

C. Surface Temperature

The CFD analysis provides the wall temperature profile as part of the solution. It is common for these vehicles to use silica and sapphire windows on the EO/IR sensors. These materials can withstand temperatures of 1270 K and 2270 K, respectively.[11] The RF sensors often contain ceramics such as silicon nitride that are exposed to surface temperatures. Silicon nitride can withstand temperatures up to 2173 K.[12]

III. Numerical Setup

To investigate the effects of hypersonic flow on signal degradation, a test case is run in air at Mach 7 and an altitude of 30 km. The exact flow conditions are described in Table 1.

Table 2. Flow Parameters

Parameter	Value
M_∞	7.00
ρ_∞	0.0180 kg/m^3
T_∞	227 K
P_∞	1170 Pa

The geometry for this case is intended to be representative of a typical hypersonic ISR platform. It consists of an axisymmetric cone that is approximately 14 meters long and 1.7 meters in radius. The geometry is depicted in Fig. 4.

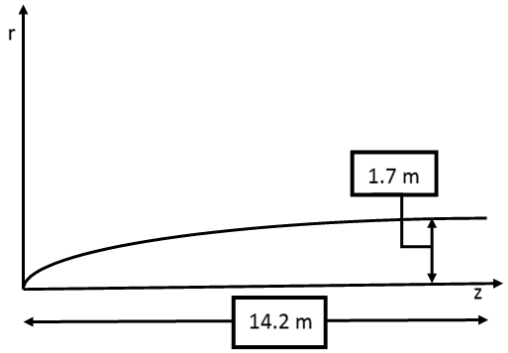

Figure 4. Simulation Geometry

These simulations employ a radiative equilibrium wall boundary condition and thermochemical non-equilibrium in the flow field. For this simulation, it is assumed that the wall emissivity is 1.0. The Menter SST model is used. Cases are run with 5 species and 11 species chemistry. For the 5 species chemistry (N_2, O_2, NO, N, and O) and the 11 species chemistry (N_2, O_2, NO, O, N, N_2^+, O_2^+, NO^+, N^+, O^+, and e^-) mechanisms, a finite-rate chemistry model is used with Park's two-temperature model.[18] To determine viscosity, Wilkes's mixing rule is used in conjunction with Blottner's curve fits. Eucken's relations are used to find thermal conductivities.

A structured mesh is created in the commercial software Pointwise. For this case, a mesh that contains approximately 29,000 cells is used. The simulations are performed on 16 processors and take 325 CPU hours, total time. It is important to note that all test cases are run on the same mesh to allow detailed comparison. The computational mesh has y+ values of less than one for cells adjacent to the wall. The mesh is shown in Fig. 5.

IV. Results

The plasma density and optical calculations are carried out along the three paths shown in Fig. 5.

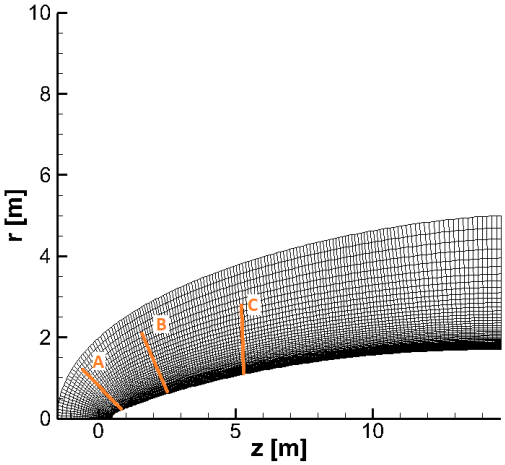

Figure 5. Paths chosen for evaluation

These paths where chosen to be representative of surface locations and directions where sensors are most likely to be used. It should be noted that in Fig. 5 the paths extend far into the flow. This is done for illustrative purposes. The calculations of effects on EO/IR sensors are confined to the boundary layer.

The general flow can be characterized by a strong shock near the stagnation point that becomes more oblique as the x coordinate increases. The flow also has a thin boundary layer contained near the wall. This is expected due to the high Reynolds number.

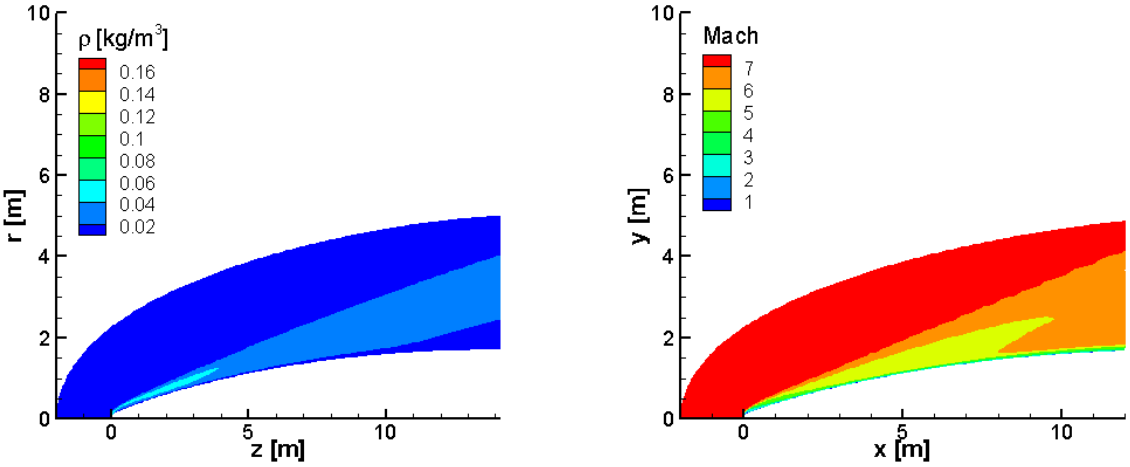

(a) **(b)**

Figure 6. Flowfield contours of (a) density, (b) Mach

The varying strength of the shock is further illustrated, in Figs. 7, 8, and 9 that show profiles of selected properties along paths A, B, and C, respectively. Figure 7 shows more rapid changes in temperature and pressure while Figs. 8 and 9 show more gradual changes.

A. EO/IR Sensor Performance

1. Method 1

The temperature and pressure profiles are extracted. Equation (4) is used to find the corrected index of refraction. This method will only predict the optical distortion from the variation of index of refraction across the boundary layer. The computational grid is not fine enough to resolve turbulent fluctuations. Therefore, this method does not directly take into consideration the fluctuating mechanisms of turbulent flow. It does, however, account for aspects such as higher wall temperatures and the resulting mean density profiles. This method will give a best case scenario. It will tell indicate the level of distortion when the turbulent fluctuations have little effect.

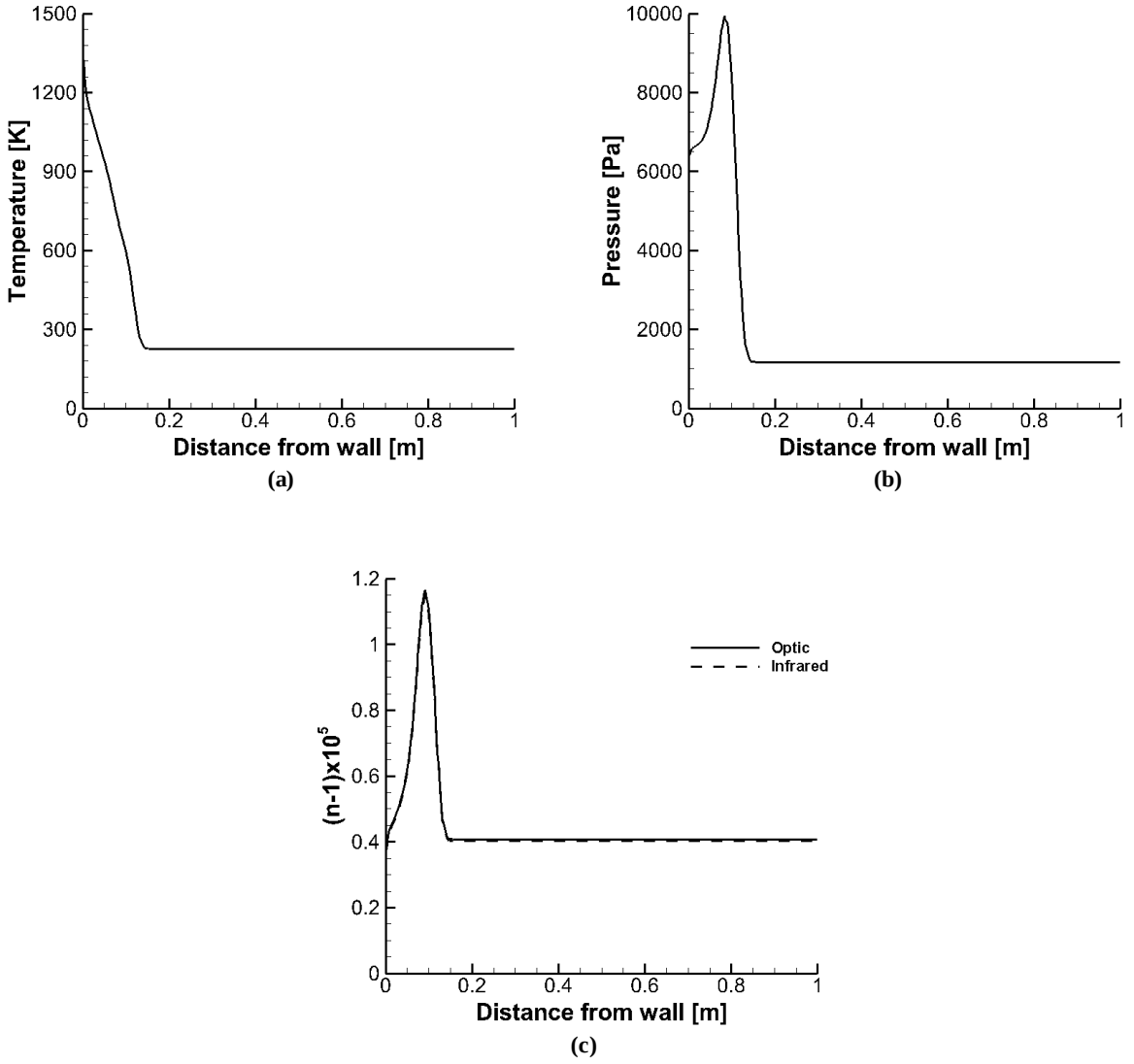

Figure 7. Temperature (a), Pressure (b) and index of refraction profiles along path A

The data extracted from Path A are shown in Fig.7. The wall temperature is elevated. This causes a slight decrease in density near the wall. The higher temperature at the wall causes species to diffuse further toward the freestream. This results in a small pressure drop near the wall, see Fig, 7 (a). All cases show that the index of refraction relies on pressure except near the wall. The n-1 profile shows a similar trend to the pressure profile.

Again, Figs. 8 and 9 show more diffuse shocks are experienced along paths B and C. These are illustrated with less severe temperature and pressure gradients.

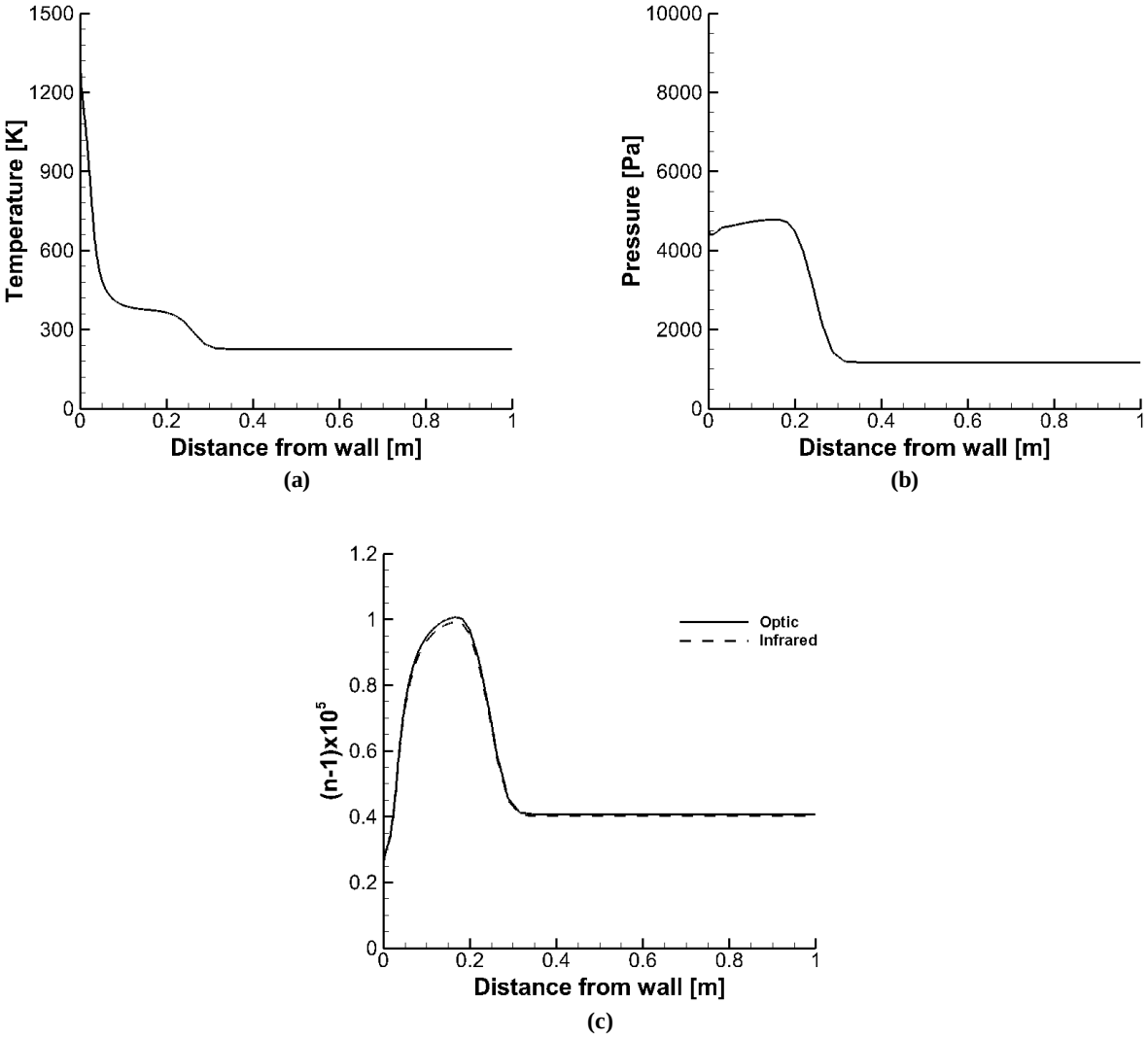

Figure 8. Temperature (a), Pressure (b) and index of refraction profiles along path B

The different gradients that each path experiences are very important. It is the gradient that is integrated over the region of interest, in this case the boundary layer, to arrive at a Strehl ratio. The data along Paths B and C follow the same trends discussed for Path A. Temperature is highest near the wall and then falls off toward the freestream. Pressure decreases slightly near the wall, increases and then decreases to the freestream value further from the wall. A main difference between paths B and C is the distance the signal must traverse inside the boundary layer. In both methods for estimating distortion, this distance is a very important part of the calculation.

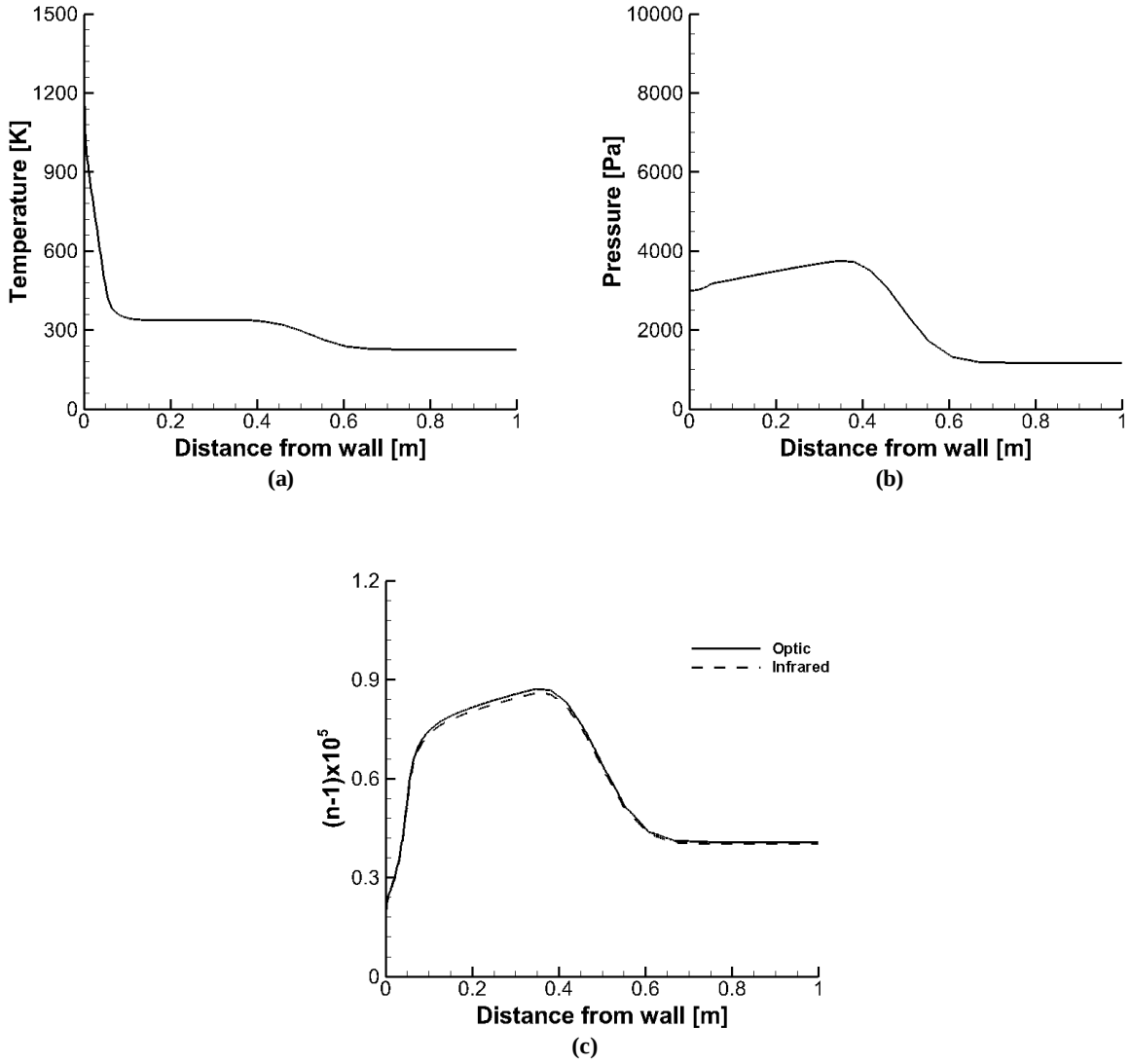

Figure 9. Temperature (a), Pressure (b) and index of refraction profiles along path C

When the data from these profiles are inserted into Eqs. (1) and (2), the Strehl ratios in Table 3 are obtained. Again, the Strehl ratio is the ratio of peak distorted image intensity to the peak intensity of an unabberated flow. Therefore, a completely undistorting flow would produce a Strehl ratio of 1.

Table 3. Strehl ratios produced by method 1

	Optical ($\lambda = 600$ nm)	Infrared ($\lambda = 2$ μm)
Path A	1.00	1.00
Path B	0.732	0.973
Path C	0.901	0.991

The Strehl ratios produced by Method 1 are largely close to 1, except for the optical signal in path B. This suggests the flow is distorted but not to a great extent. As stated earlier, Method 1 provides the best case scenario because it does not directly account for turbulent fluctuations. For this reason, another method is investigated.

2. Method 2

Method 2 is adapted from an algebraic equation presented in Wyckham.[2] The same paths are used as in method 1. The calculation of the Strehl ratios is conducted using Eqs. (7) and (9). Table 4 shows the Strehl ratios produced by this method.

Table 4. Strehl ratios produced by method 2

	Optical ($\lambda = 600$ nm)	Infrared ($\lambda = 2$ μm)
Path A	0.951	0.996
Path B	0.036	0.749
Path C	0.155	0.851

As expected, this method produces lower Strehl ratios than Method 1. It is therefore important to include the fluctuations' effects. However, it is likely that this method under predicts Strehl ratios of 0.3 or below.[2] This method is also highly dependent on distance the signal must traverse in the boundary layer. This explains the low Strehl ratio for path B, which travels the largest distance in the boundary layer since its path in slightly angled.

B. RF Sensors

The plasma density is explored along the same paths that are utilized for the EO/IR analysis. The three density profiles are shown in Fig. 10. Path C experiences the highest density with a peak number density of 4.22×10^8 m^{-3}. Using this peak value, Eq. (11) is used to find the radio frequency below which the signal will be distorted. An RF signal of 1.8×10^5 Hz or lower would be obscured if it traverses Path C.

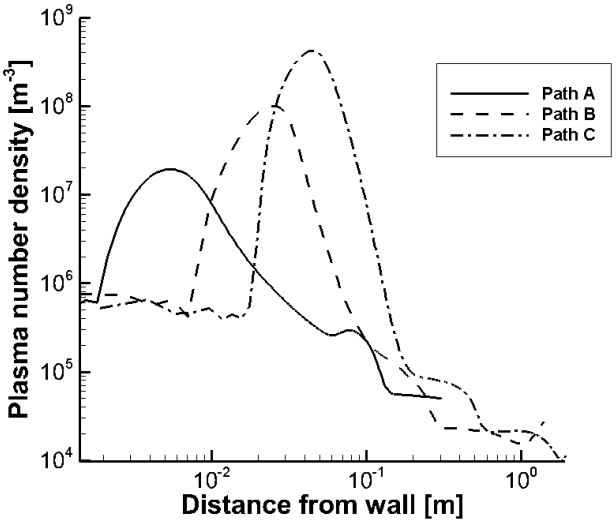

Figure 10. Plasma number density along the three paths

This is well below the frequencies used in most sensor applications (see Table 1). The lowest frequency of interest is two orders of magnitude larger. Furthermore, the highest plasma density over the entire geometry in this study is 1.09×10^9 m^{-3}. This is a critical density for signals of 2.97×10^5 Hz and lower which is also well below the frequencies discussed in table 1. Another simulation is run at an altitude of 20 km. This only increased the frequency that will be distorted to 7.5×10^5 Hz.

C. Surface Temperature

The profile of temperature along the vehicle surface obtained in the simulation is shown in Fig. 11. The peak surface temperature is approximately 1600 K.

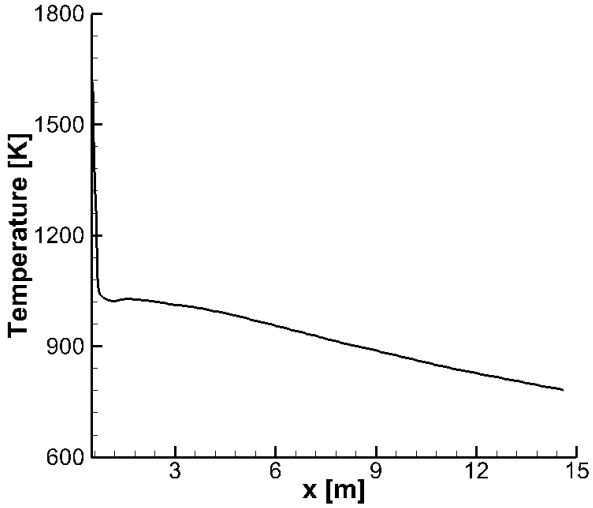

Figure 11. Surface temperature profile

As expected, the peak temperature is at the stagnation point. As long as a silica window is not used at the stagnation point, the temperature of the vehicle's surface is unlikely to cause any type of degradation. The silicon nitride and sapphire windows that can withstand temperatures above 2000 K can be placed anywhere on this vehicle.

V. Conclusion and Future Work

When traveling at hypersonic speeds, a number of different flow phenomena must be considered. These phenomena may impact ISR sensor performance. Three different types of sensor interference were considered in this study. EO/IR aberrations, RF signal degradation, and elevated surface temperatures were analyzed to determine if they are significant. For the Mach 7, 30 km altitude case considered, it was determined that optical and infrared signals may be highly distorted when traversing the boundary layer. Further work is needed to assure that the methods used to assess aberrations are accurately accounting for all turbulent flow phenomena. For example, the existing equation in Method 2 does not account for the anisotropy that is inherent in turbulence. A study showed that the differing turbulent structures affect the distortion in different manners. [3] The hairpin vortices are particularly detrimental to optical signals.[3] In order to better account for the anisotropy, a conservation equation for the turbulent density fluctuations can be constructed and solved alongside the other flow equations. [14] The density fluctuations can be integrated along a path of interest to allow the OPD and Strehl ratio to be calculated. This will allow a measure of anisotropy to be accounted for while still allowing for the efficient calculation of flow data for high Reynolds number flows. It will also allow extension of this method to many other geometries, especially those with significant pressure gradients in the normal direction.

This study also showed that at these conditions it is unlikely that there will be interference with RF signals. However, this study focused on high altitude flight. Higher Mach numbers should also be studied. The Mach number would lead to increased flow temperature around the vehicle which would promote dissociation and ionization. The increased plasma density would obstruct more frequencies.

The final aspect of this study was an analysis of the surface temperature. This investigation yielded surface temperatures that would not degrade the sensor windows unless the sensor is placed on or near the stagnation region. The particular material properties of the sensor windows should be included in future simulations such as emissivity and thermal conductivity.

References

[1]Kim, M., "Electromagnetic Manipulation of Plasma Layer for Re-Entry Blackout Mitigation," Doctoral Thesis, Department of Aerospace Engineering, University of Michigan, Ann Arbor, MI, 2009.

[2]Wyckham, C. and Smits, A., "Aero-Optic Distortion in Transonic and Hypersonic Turbulent Boundary Layers," AIAA Journal, Vol. 47, No.9, Sept. 2009.

[3]Weng, M., Mani, A., Stanislav, G., "Physics and Computation of Aero-Optics," Annual Review of Fluid Mechanics, Vol. 44, 2012, pp. 299-321.

[4] Rybak, J., "Causes, Effects and Diagnostic Measurements of the Reentry Plasma Sheath," Defense Technical Report AD718428, Colorado State University, Fort Collins, Co, December 1970.

[5]Martin, A., Scalabrin, L.C., and Boyd, I.D., "High Performance Modeling of Atmospheric Re-entry Vehicles," Journal of Physics: Conference Series, Vol. 341, 2012, Article 012002.

[6]Menter, F., "Improved Two-Equation k-omega Turbulence Models for Aerodynamic Flow," NASA STI/Recon Technical Report, October 1992.

[7]Spalart, P.R. and Allmaras, S.R., "A One Equation Turbulence Model for Aerodynamic Flows," Recherche Aerospatiale, No.1, 1994, pp.5-21.

[8]Born, M. and Wolf, E., *Principles of Optics*, Permagon Press, 1975, p. 464.

[9]Baxter, M.R., Truman, C.R., and Masson, B.S., "Predicting the Optical Quality of Supersonic Shear Layers," AIAA Paper 1988-2771, June 1988.

[10]Koretsky, G.M., Nicoll, J.F., and Taylor, M.S., "A Tutorial on Electro-Optical/Infrared (EO/IR) Theory and Systems," Institute for Defense Analyses Document D-4642, January 2013.

[11]Handbook of Chemistry and Physics, Edited by David R. Lide, CRC Press, 1996, p. 10-304.

[12]"Silicon Nitride" MSDS Item # SI-501, Mallinckrodt Baker: Phippsburg, NJ. April 2011.

[13]Wang, K. and Wang, M., "Aero-optics of Subsonic Turbulent Boundary Layers," Journal of Fluid Mechanics, Vol. 696, 2012, pp. 122-151.

[14]JingYuan, L., "A Three-Equation Turbulence Model for High-Speed Flows," Science China:Technological Sciences, Vol. 56, No.803-811, April 2013.

[15]White, F., Viscous Fluid Flow, 3rd ed., McGraw-Hill, New York, 2006, Ch. 4, pp.228.

[16]Gordeyev, S., Rennie, M., "Aero-Optical Measurements of High-Mach Supersonic Boundary Layers," AIAA-2015-3246, June 2015.

[17]Yanta, W. J., Spring, W. C., III, Lafferty, J. F., Collier, S. C., Bell, R. L., Neal, D., Hamrick, D., Copland, J., Pezzaniti, L., Banish, M., and Shaw, R., "Near-and Far-Field Measurements of Aero-Optical Effects due to Propagation Through Hypersonic Flows," AIAA Paper 2000- 2357, 2000.

[18]Park, C. Nonequilibrium Hypersonic Aerothermodynamics. John Wiley & Sons, 1990.